A ternary Pt/MnO₂/graphene nanohybrid with an ultrahigh electrocatalytic activity toward methanol oxidation

Huajie Huang [a,b], Qun Chen [b], Mingyang He [b], Xiaoqiang Sun [b], Xin Wang [a,*]

[a] Key Laboratory of Soft Chemistry and Functional Materials, Nanjing University of Science and Technology, Ministry of Education, Nanjing 210094, China
[b] Key Laboratory of Fine Petrochemical Engineering, Changzhou University, Changzhou 213164, China

HIGHLIGHTS

- A ternary Pt/MnO₂/graphene nanohybrid is synthesized for the first time.
- Graphene can be used as both a green reductant and an ideal substrate.
- Ultrafine Pt nanoparticles are highly dispersed on MnO₂-modified graphene sheets.
- Pt/MnO₂/graphene shows an ultrahigh catalytic activity toward methanol oxidation.

ARTICLE INFO

ABSTRACT

Ultrafine Pt nanoparticles with an average diameter of only 1.7 nm are uniformly dispersed onto MnO_2-functionalized graphene sheets by a facile and cost-effective method. In such a ternary Pt/MnO₂/graphene sheets (Pt/MnO₂/GS) nanohybrid, each component provides unique and critical function to achieve optimized utilization of metallic platinum, allowing it to express ultrahigh electrocatalytic activity ability in methanol oxidation (the forward anodic peak current density is up to 1224 mA mg^{-1}) in comparison with Pt/graphene sheets (Pt/GS), Pt/Vulcan XC-72 (Pt/XC-72) and Pt/MnO₂/XC-72 catalysts. This work could provide new insights into the fabrication of the next generation high-performance electrocatalyst and promote their practical application in fuel-cell technologies.

© 2013 Elsevier B.V. All rights reserved.

1. Introduction

Direct methanol fuel cells (DMFCs) as promising alternative power sources have attracted considerable attention due to their merits of high theoretical energy conversion efficiency, low pollutant emission, and convenient storage and transport of liquid fuel [1–3]. Platinum is the best-known precious metal catalyst that exhibits significant electrocatalytic activity for methanol oxidation [4,5]. However, given the limited resources and high cost of platinum, it is very necessary to improve the utilization efficiency of noble metals and lower the cost for the practicality and commercialization of DMFCs. In this regard, hybrid electrode materials in which metal Pt are embedded in other elements such as Ru, Ni, Co, Mn, Zn etc. or oxides RuO₂, CeO₂, TiO₂ etc. have been widely studied and demonstrated much improved electrocatalytic performance

toward methanol oxidation [6–16]. Among them, MnO₂ is of particular interest due to its excellent proton conductivity, low cost, environmental friendliness, and natural abundance [17,18]. Nevertheless, challenging issues such as the uneven distribution of Pt nanoparticles (NPs), the poor electric conductivity of MnO₂ and the relatively cumbersome preparation procedure, are the critical obstacles that hinder the further application of hybrid Pt/MnO₂ catalysts [19,20]. Therefore, demand for overcoming these obstacles has led to extensive efforts to explore facile routes to obtain Pt/MnO₂ hybrid with more advanced structural design.

On the other hand, in order to further maximize the catalytic activity and minimize the amount of precious Pt, another efficient way to achieve better utilization of Pt nanostructures is to disperse them onto high surface area carbon supports, which can not only provide large accessible surface areas for fast transport of reactants to the electrocatalysts but also facilitate the charge transportation during the methanol oxidation reactions [21–23]. In recent years, graphene, a single layer of sp²-bonded carbon atoms tightly packed into a two-dimensional honeycomb structure, is conceived as an

* Corresponding author. Tel.: +86 25 8431 5943; fax: +86 25 8431 5054.
  E-mail addresses: wangx@mail.njust.edu.cn, wxin48@163.com (X. Wang).

extremely promising catalyst support in DMFCs [24−27]. Apart from its potential for low-cost, there are several attributes of the 2D-planar structure material that are very unique when compared to traditional materials, such as the large theoretical specific surface area, intrinsically superior electronic conductivity and excellent chemical stability [28]. However, the combination of graphene sheets (GS) with Pt alone can not be conducive to achieving the maximum utilization of metallic platinum.

In our previous works, we reported synthesis and properties of MnO_2−graphene and Pt−graphene nanocomposites [29−33]. It is of great interest to study the possibility of Pt−MnO_2−graphene ternary composites. If that can be accomplished, then it may be possible to obtain some exceptional properties as a result of the interaction of Pt, MnO_2 and graphene sheets as well as the concerted effect. Recently, Liu et al. showed that the Pd/MnO_2/ graphene composite exhibited enhanced activity and stability for catalyzing methanol oxidation in alkaline media [34]. It is noted that the distribution of MnO_2 NPs on the surface of the graphene sheets was not uniform and a number of MnO_2 aggregates could be observed, which will probably result in a large loss of metal (Pd) activity. Moreover, the preparation procedure of Pd/MnO_2/graphene is relatively cumbersome and various reducing agents (such as ethylene glycol and excess $NaBH_4$) were used.

Herein, we report a simple and cost-effective strategy for the synthesis of a ternary Pt/MnO_2/GS composite as an advanced electrocatalyst for high-performance DMFCs. As shown in Scheme 1, graphene oxide (GO) was prepared from powdered flake graphite by a modified Hummers' method [35,36]. With the introduction of $KMnO_4$ aqueous solution into the GO dispersion system, the carbon atoms of graphene framework would reduce $MnO_4^−$ in situ to form MnO_2 in a water-containing system at room temperature [30,37,38]. The whole process is proposed to involve the reaction: $4KMnO_4 + 3C + H_2O \rightarrow 4MnO_2 + K_2CO_3 + 2KHCO_3$. Thereafter, Pt$(NO_3)_2$ was added to the MnO_2/GO nanosheets colloid suspension under stirring. During the solvothermal reaction, both of the reduction of graphene oxide and Pt NPs loading can be achieved, leading to the formation of Pt/MnO_2/GS composite. Pt/GS, Pt/XC-72 (commercial carbon black, Vulcan XC-72) and Pt/MnO_2/ XC-72 were also synthesized for comparison.

2. Experimental

2.1. Materials

Natural flake graphite with an average particle size of 40 μm was purchased from Qingdao Zhongtian Company (Qingdao, China). Vulcan XC-72 was purchased from Cabot Corp. Pt$(NO_3)_2$ solution was obtained from Shanghai July Chemical Co. Ltd. (Shanghai, China). Nafion 117 was purchased from Dupont. All other chemicals employed were of analytical grade and used as received. All aqueous solutions were prepared using deionized water.

2.2. Synthesis of MnO2/graphene oxide (MnO2/GO) and MnO2/ Vulcan XC-72 (MnO2/XC-72) composites
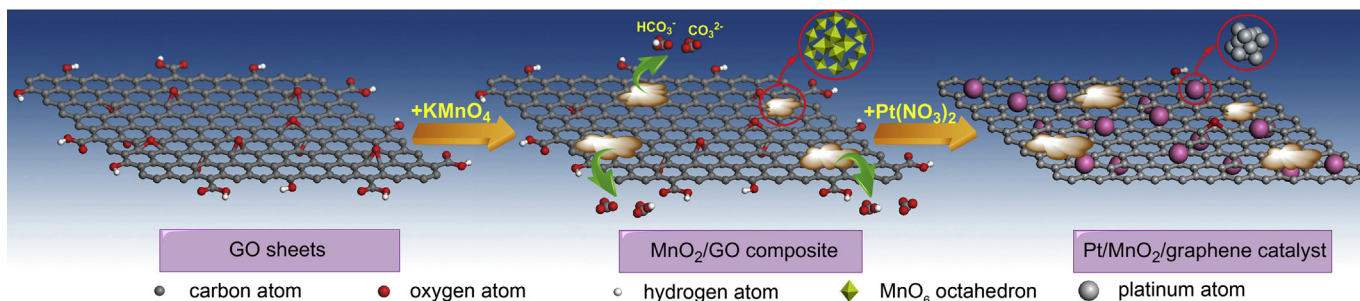
GO was prepared from powdered flake graphite by a modified Hummers' method as described previously [35,36]. GO (400 mg) was dispersed in 600 mL of water to obtain a yellow−brown aqueous solution with ultrasonication for 0.5 h. As to the deposition of hydrous MnO_2 on GO sheets, 600 mL of as-obtained GO dispersion was vigorously stirred, then 20 mL of a $KMnO_4$ solution (158 mg of $KMnO_4$ dissolved in 20 mL of de-ionized water) was added rapidly. The resulting solution was kept standing in a covered beaker under ambient conditions for 12 h. During the reaction, the purple color of the mixture faded gradually and no obvious precipitation occurred. As-generated product, labeled as MnO_2/GO, was centrifuged, washed, and dried in air at 60 °C overnight. The synthesis of MnO_2/XC-72 was similar to that of MnO_2/GO with the GO replaced by Vulcan XC-72.

2.3. Synthesis of Pt/MnO2/graphene sheets (Pt/MnO2/GS), Pt/ graphene sheets (Pt/GS), Pt/Vulcan XC-72 (Pt/XC-72) and Pt/MnO2/ Vulcan XC-72 (Pt/MnO2/XC-72) composites

In a typical synthesis route, MnO_2/GO (20 mg) was dispersed in 30 mL of water and 50 mL of ethylene glycol by sonication for 1 h. Then 0.035 mL of 0.73 M Pt$(NO_3)_2$ was introduced to the solution with magnetic stirring for 15 min. The resulting suspension was transferred into a 100 mL Teflon-lined stainless steel autoclave and sealed tightly. The autoclave was then heated to 120 °C and kept there for 12 h. After the solvothermal treatment, the nanocomposite, denoted as Pt/MnO_2/GS, was centrifuged, washed, and finally dried in air at 60 °C overnight. For comparison, deposition of Pt nanoparticles on graphene sheets, Vulcan XC-72, and MnO_2/XC-72 was also achieved by the similar procedure and the composites were denoted as Pt/GS, Pt/XC-72 and Pt/MnO_2/XC-72, respectively. The exact loadings of metal Pt in Pt/MnO_2/GS, Pt/GS, Pt/XC-72 and Pt/MnO_2/XC-72 samples were measured at 22.1, 18.3, 19.4 and 20.9 wt% Pt, respectively. The weight ratio between MnO_2 and the GS was estimated to be 6.7:100.

2.4. Characterization

Powder X-ray diffraction (XRD) analyses were performed on a Bruker D8 Advance diffractometer with Cu Kα radiation ($\lambda \approx 1.54$ Å). The patterns were obtained using a step size of 0.05° 2θ and 0.1 s per step. Raman spectra of all the samples were collected using a Renishaw Raman microscope. X-ray photoelectron spectra (XPS) were recorded on a RBD upgraded PHI-5000C ESCA system (Perkin Elmer) with Al Kα radiation ($h\nu = 1486.6$ eV). Fourier transform infrared (FT-IR) spectra were recorded on a Shimadzu IR Prestige-21 spectrometer. Ultraviolet−visible (UV−vis) absorption spectra were collected using a BRAIC UV-1201 spectrophotometer.

- carbon atom
- oxygen atom
- hydrogen atom
- MnO_6 octahedron
- platinum atom

GO sheets | MnO_2/GO composite | Pt/MnO_2/graphene catalyst

Scheme 1. Illustrations of the synthesis of Pt/MnO_2/graphene catalyst.

Transmission electron microscopy (TEM) images and energy dispersive X-ray (EDX) spectroscopy were performed on a JEOL JEM-2100 microscope operating at 200 kV, by depositing a drop of sample dispersion onto 300 mesh Cu grids coated with a carbon layer. The Pt loadings of the catalysts were accurately determined with a Perkin Elmer ELAN9000 inductively couples plasma mass spectrometer (ICP-MS).

2.5. Electrochemical measurements

Electrocatalytic activities of samples were measured in a conventional three electrode cell using a CHI 660B electrochemical workstation. The three-electrode cell consisted of a Pt wire serving as the counter electrode, a saturated calomel electrode (SCE) serving as the reference electrode and a glassy carbon (GC) disk (3 mm in diameter) with coated catalysts serving as the working electrode. The work electrode was manufactured as follows: 2 mg of catalyst powder was dispersed in a mixed solution (500 μL of water, 500 μL of ethanol and 50 μL of 5% Nafion 117 solution) with ultrasonication for 30 min to form a homogeneous black suspension. Then 6 μL of the resulting suspension was carefully pipetted onto the GC electrode surface, and the coating was dried at room temperature for 1 h. Therefore, the loading amounts of metal platinum on the electrodes for Pt/MnO$_2$/GS, Pt/GS, Pt/XC-72 and Pt/MnO$_2$/XC-72 catalysts were 0.038, 0.031, 0.033 and 0.036 mg cm^{-2}, respectively. The ECSA values of the catalysts were determined by cyclic voltammetry (CV) of the hydrogen absorption/desorption in 1 M H$_2$SO$_4$ solution at room temperature. The electrocatalytic activity of the as-prepared catalysts for the methanol oxidation was characterized by collecting CVs in a N$_2$-purged 1 M H$_2$SO$_4$ and 2 M methanol solution at a scan rate of 20 mV s^{-1}. Several activation scans were performed until reproducible voltammograms were obtained. Only the last voltammograms were used for comparing the catalytic activity of the specified catalysts. The chronoamperometry tests were conducted at 0.5 V for a period of

30 min. The chronopotentiometric curves were recorded in 1 M H$_2$SO$_4$ and 2 M methanol solution. The value of the applied current was obtained at 0.45 V from the forward scan of the corresponding cyclic voltammogram. Electrochemical impedance spectra (EIS) were recorded at frequencies from 10^5 to 0.02 Hz in a solution of 2 M methanol and 1 M H$_2$SO$_4$, and the amplitude of modulation potential was 10 mV.

3. Results and discussion

Typical XRD patterns of graphite oxide, MnO$_2$/GO, Pt/MnO$_2$/GS, Pt/GS and Pt/XC-72 are presented in Fig. 1a. Compared with the XRD pattern of graphite oxide (spectrum 1), the characteristic diffraction peak (002) at $2\theta = 10.5°$ almost disappeared after the introduction of MnO$_2$ (spectrum 2), indicating the exfoliation of GO sheets, while the other diffraction peaks of MnO$_2$/GO are similar to those of α-MnO$_2$ (JCPDS No. 44-0141). Moreover, as has been demonstrated in previous studies, the broad diffraction pattern detected at 2θ between 15° and 35° can be interpreted as scattering from an individual MnO$_2$ layer, which is a clue of the formation of the layered MnO$_2$ lamellas [37,39,40]. It should be noted that the electrochemical activity of MnO$_2$ depends to a great extent on its structure and morphology [41,42]. In this respect, layered MnO$_2$ lamellas have incurred intense interest because of their high surface area, low density, and good permeation [40,43]. After the subsequent loading of Pt to the MnO$_2$/GO nanosheets, as displayed in spectrum 3, some MnO$_2$ diffraction peaks are covered by those of the face-centered-cubic (fcc) structure of Pt; however, the characteristic (110), (200), (310) and (541) planes of MnO$_2$ can still be observed. Furthermore, the full width at half maximum (FWHM) of the diffraction peaks of Pt/MnO$_2$/GS is wider than those of Pt/GS and Pt/XC-72 (spectrum 4 and 5, respectively), implying the smaller particle size of the Pt NPs supported on the MnO$_2$/GS supports. The fine structures of graphite oxide, MnO$_2$/GO and Pt/MnO$_2$/GS were further investigated by Raman spectroscopy. As can be seen from
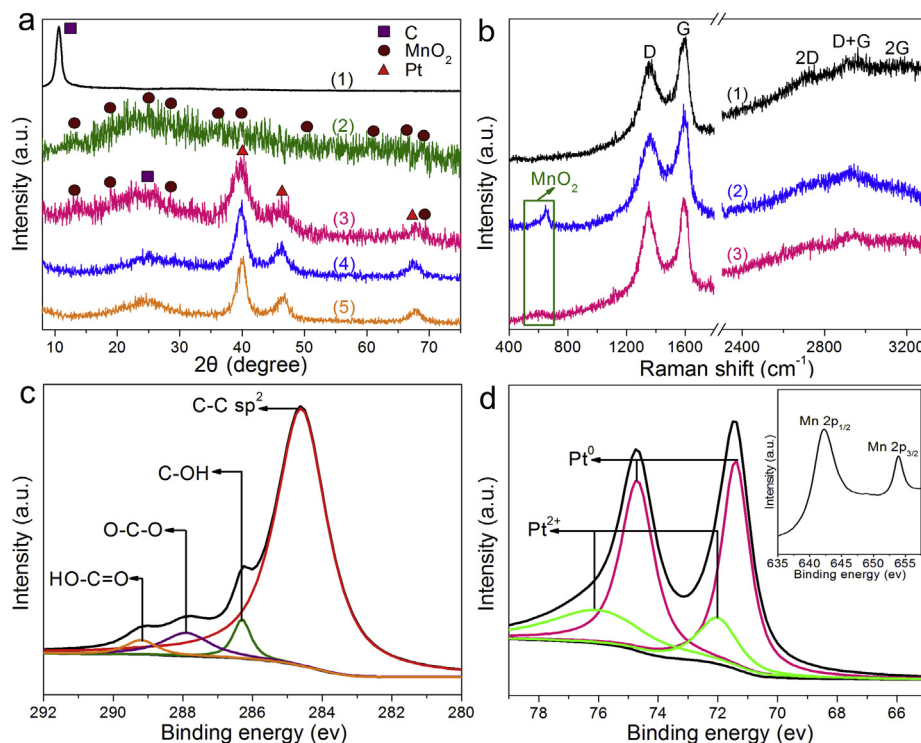
Fig. 1. (a) XRD patterns of (1) graphite oxide, (2) MnO$_2$/GO, (3) Pt/MnO$_2$/GS, (4) Pt/GS and (5) Pt/XC-72. (b) Raman spectra of (1) graphite oxide, (2) MnO$_2$/GO and (3) Pt/MnO$_2$/GS. (c) C 1s, (d) Pt 4f and the inset of (d) Mn 2p core-level XPS spectra of Pt/MnO$_2$/GS.

Fig. 1b, the Raman peaks appearing at around 1350 and 1570 cm^{-1} correspond to the poor crystallization of graphite (D-band) and the stretching mode of crystal graphite (G-band), respectively [44]. As for Pt/MnO$_2$/GS, the increased D/G intensity ratio suggests a decrease in the average size of the sp^2 domains upon reduction of the exfoliated GO [45]. It is noteworthy that overtone (2D and 2G) and combination bands (D + G) associated with the graphitic phases are also evident in all spectra and the peak position (2690 cm^{-1}) of the 2D band is similar to that of a mono-layer graphene [46]. Meanwhile, the weak bands located at 570 and 640 cm^{-1} in spectrum 2 and 3 are due to the symmetric stretching vibration (Mn–O) of the MnO$_6$ groups, which confirm the yield of MnO$_2$ by replacing part of the carbon atoms in the framework of graphene [47].

Further information on the composition of the as-prepared composites was obtained from XPS measurements. As shown in Fig. 1c and Fig. S1, the intensity of oxygen-containing groups such as C–OH (286.1 eV), C–O–C (287.6 eV), H–O–C=O (288.9 eV) in Pt/MnO$_2$/GS was obviously reduced during the solvothermal reaction, while the peak at 284.5 eV, C–C bond, became predominant (Table S1) [27]. The significantly lower O/C ratio in the composite can be linked to the much faster rate of charge transfer, which is favorable for the oxidation of methanol. XPS analysis also shows that there are different Pt oxidation states in the catalyst. It can be seen from Fig. 1d that the Pt 4f signal of Pt/MnO$_2$/GS represents the sum of two pairs of doublets: the most intense doublet (71.4 and 74.7 eV) is due to metallic Pt and the second doublet (72.0 and 76.0 eV) can be ascribed to the +2 oxidation state of Pt [15]. In addition, the Mn 2p XPS spectrum of the Pt/MnO$_2$/GS composite exhibits two characteristic peaks at 642.2 eV and 654.0 eV, corresponding to the Mn 2p$_{3/2}$ and Mn 2p$_{1/2}$ spin-orbit peaks of α-MnO$_2$, respectively (the inset of Fig. 1d) [48]. These conclusions are also supported by the results from EDX, FT-IR and UV–vis analysis (Figs. S2–S4, respectively). Thus it is safe for us to derive that α-MnO$_2$, graphene and crystalline Pt coexist in the prepared nanohybrid.

Fig. 2 depicts transmission electron microscopy (TEM) images of the MnO$_2$/GO, Pt/MnO$_2$/GS, Pt/GS and Pt/XC-72 nanohybrids. TEM images with higher magnifications of these nanohybrids are provided in Supporting information (Fig. S5). As shown in Fig. 2a, it was found that the almost transparent GO sheets were thinly covered with well-dispersed layered MnO$_2$. No obvious stacking of these MnO$_2$ lamellas was observed, mainly due to the fact that the formed MnO$_2$ coating could function as a barrier preventing further access of the MnO$_4^-$ ions to the functionalized carbon surface [31,38]. Afterward, MnO$_2$-functionalized GO sheets were used to load Pt NPs for producing ternary Pt/MnO$_2$/GS composite, as displayed in Fig. 2b. The most striking feature is that the ultrafine Pt metal NPs with diameters less than 3 nm were uniformly distributed on the surface of MnO$_2$/GS sheets. Lattice fringes of both the (111) plane in face-centered cubic Pt (0.22 nm) and the (400) plane in α-MnO$_2$ (0.24 nm) are shown in the high-resolution TEM (HRTEM) image (the inset of Fig. 2b), which correlate well with the XRD results. In Fig. 2c and d, it is clearly seen that Pt NPs were also deposited on GS and XC-72 supports, however, their distributions become much broader than those on MnO$_2$/GS surfaces and the aggregation of some Pt NPs even took place. The statistical size analysis of Pt NPs indicates that the average particle sizes are about 1.7 nm, 3.6 nm and 4.7 nm for Pt/MnO$_2$/GS, Pt/GS and Pt/XC-72, respectively (Fig. 2e). The findings can be explained in terms of the reasons that for Pt/MnO$_2$/GS, the direct carbon–MnO$_4^-$ reactions occur preferentially at the defective sites in GO, and therefore a significant amount of framework defects were consumed in the first step and the residual carbon–oxygen functional groups on MnO$_2$/GO sheets played an important role in dispersing Pt NPs. Moreover, the presence of hydrous MnO$_2$ can create large hydrophilic regions on the surface of GO, which can facilitate the diffusion of Pt^{2+} ions and effectively prevent the metal NPs from agglomeration [19]. However, in the case of Pt/GS, although plenty of oxygen-containing groups on GO can promote the deposition of Pt NPs, the uneven distribution of excessive
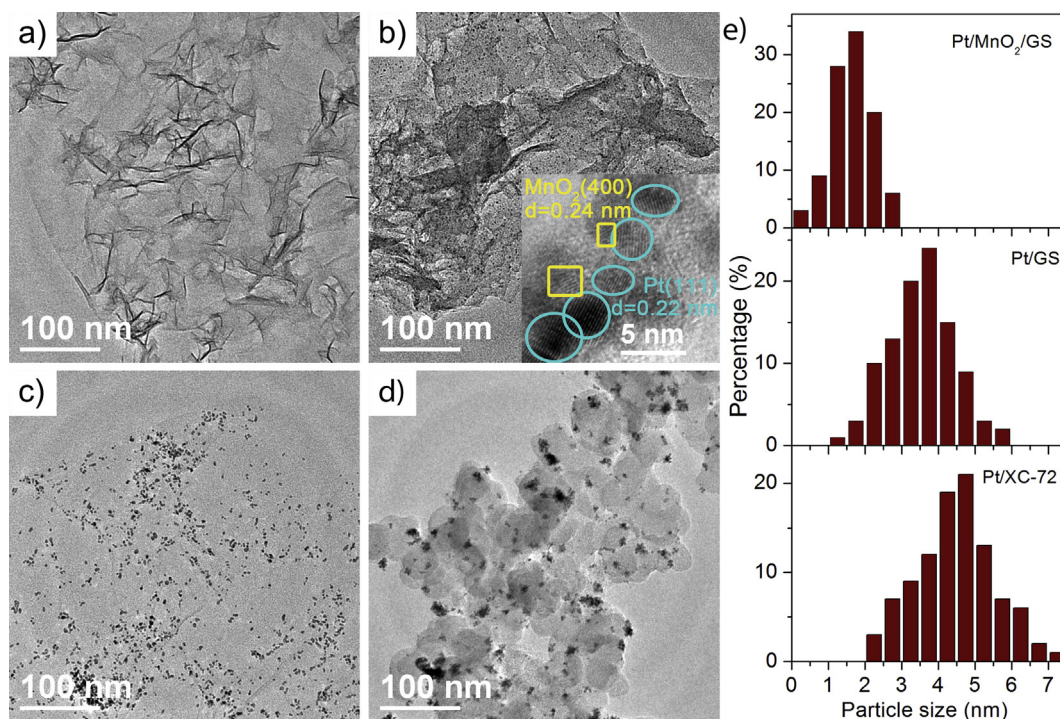

Fig. 2. TEM images of (a) MnO$_2$/GO, (b) Pt/MnO$_2$/GS, (c) Pt/GS and (d) Pt/XC-72. The inset of (b) is an HRTEM image of Pt/MnO$_2$/GS. (e) The histograms of Pt particle size distribution of different carbon-based samples.

groups resulted in extensive aggregation of Pt NPs on reduced-GO surface. As for Pt/XC-72, the poor dispersion of Pt NPs is probably caused by the relatively smaller specific area of XC-72.

To explore the potential applications, the as-obtained Pt/MnO$_2$/GS hybrid was tested as a nanoelectrocatalyst for oxidation of methanol to evaluate its catalytic activity. By measuring the charge collected in the hydrogen adsorption/desorption region after double-layer correction, the electrochemically active surface area (ECSA) of Pt/MnO$_2$/GS was calculated to be as high as 103.2 m^2 g^{-1}, more than 2 times as large as that for Pt/GS (49.1 m^2 g^{-1}), nearly 3 times the Pt/XC-72 (38.5 m^2 g^{-1}) and 2 times the Pt/MnO$_2$/XC-72 (54.4 m^2 g^{-1}) catalyst (Fig. 3a and Table S2), demonstrating that the Pt/MnO$_2$/GS electrocatalyst not only possesses a larger number of catalytically active sites available, but also is electrochemically more accessible, which are essential for the electrocatalytic re-actions. This remarkable improvement can be primarily attributed to the concerted effect of MnO$_2$ nanolamellas and graphene sheets and the high dispersion of small-sized Pt NPs on modified carbon sheets. Fig. 3b presents the cyclic voltammograms (CVs) of the electrodes coated with the Pt/MnO$_2$/GS, Pt/GS, Pt/XC-72 and Pt/MnO$_2$/XC-72 catalysts in a 1 M H$_2$SO$_4$ solution containing 2 M CH$_3$OH. It can be seen that the Pt/MnO$_2$/GS catalyst exhibits an ultrahigh forward peak current density of 1224 mA mg^{-1}, which is significantly higher than the one obtained from Pt/GS (357 mA mg^{-1}), Pt/XC-72 (225 mA mg^{-1}), Pt/MnO$_2$/XC-72 (435 mA mg^{-1}), PtRu/CNT (~260 mA mg^{-1}) [49], Pt/CeO$_2$/graphene (366 mA mg^{-1}) [50], Pt/MnO$_2$/CNT (431 mA mg^{-1}) [19], Pt/mesoporous CNTs (~450 mA mg^{-1}) [51], and recent state-of-art Pt-based nanomaterials such as Pt/ionic liquid/CNT (~410 mA mg^{-1}) [52], Pt-on-Pd bimetallic nanodendrite (490 mA mg^{-1}) [53], PtRu/N-doped CNT/graphene (500 mA mg^{-1}) [54], Pt-on-Pd bimetallic nanodendrite/graphene (647 mA mg^{-1}) [55], Pt/RuO$_2$·xH$_2$O/CNT (~720 mA mg^{-1}) [14]. To gain further insight into the specific ac-tivities of different catalysts, the electrochemical data have also been normalized to the electrochemical surface area. In comparison

with the Pt/GS (0.73 mA cm^{-2}), Pt/XC-72 (0.58 mA cm^{-2}) and Pt/MnO$_2$/XC-72 (0.80 mA cm^{-2}) catalysts, Pt/MnO$_2$/GS (1.19 mA cm^{-2}) showed ~63%, ~105% and ~49% increment of the specific activity, respectively, giving clear evidence that the utility of MnO$_2$/GS sheet also substantially increase the catalytic activity per unit sur-face area of Pt. Additionally, as indicated by the dashed line in Fig. S6, the corresponding oxidation potential of the Pt/MnO$_2$/GS hybrid was obviously lower than those of reference catalysts at a given oxidation current density, implying methanol oxidation was catalyzed more easily on the Pt/MnO$_2$/GS hybrid. It is well known that the ratio of peak current in the positive scan (I_f) versus the backward negative scan (I_b) can be used to describe the catalyst tolerance to the intermediate carbonaceous species accumulated on the electrode surface [26,27]. As listed in Table S2, the Pt/MnO$_2$/GS hybrid shows the highest I_f/I_b ratio of 1.23, hence suggesting an effective removal of the poisoning species from the Pt/MnO$_2$/GS surface. This arises from the fact that the existence of MnO$_2$ nanolamellas on graphene sheets can provide abundant hydroxyl sources for oxidation of CO-like intermediate species at lower po-tentials [34].
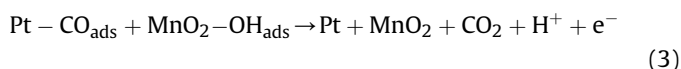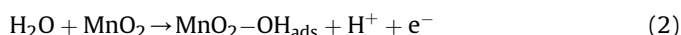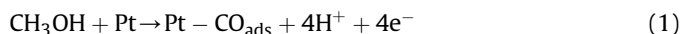
The long-term electrocatalytic activities and stabilities of Pt/MnO$_2$/GS, Pt/GS, Pt/XC-72 and Pt/MnO$_2$/XC-72 were examined by chronoamperometry for methanol oxidation at 0.5 V for 2000 s. It is evident from Fig. 3c that the Pt NPs supported on MnO$_2$-func-tionalized graphene sheets exhibit a much slower current decay over the entire time range relative to the Pt/GS, Pt/XC-72 and Pt/MnO$_2$/XC-72 electrocatalysts, indicating a remarkably durable cat-alytic activity of Pt/MnO$_2$/GS. After the electrochemical experi-ments, the structural integrity of the Pt/MnO$_2$/GS composite was overall preserved with no obvious deterioration and the Pt NPs can still keep the well structure of the (111) crystalline plane (Fig. S7a and b). Meanwhile, the EDX analyses (Figs. S2c and S7c) show that there is no significant change in the atomic ratio of Pt/Mn for the Pt/MnO$_2$/GS composite (~2:1) after electrochemical measurements. These results sufficiently prove that MnO$_2$-functionalized graphene
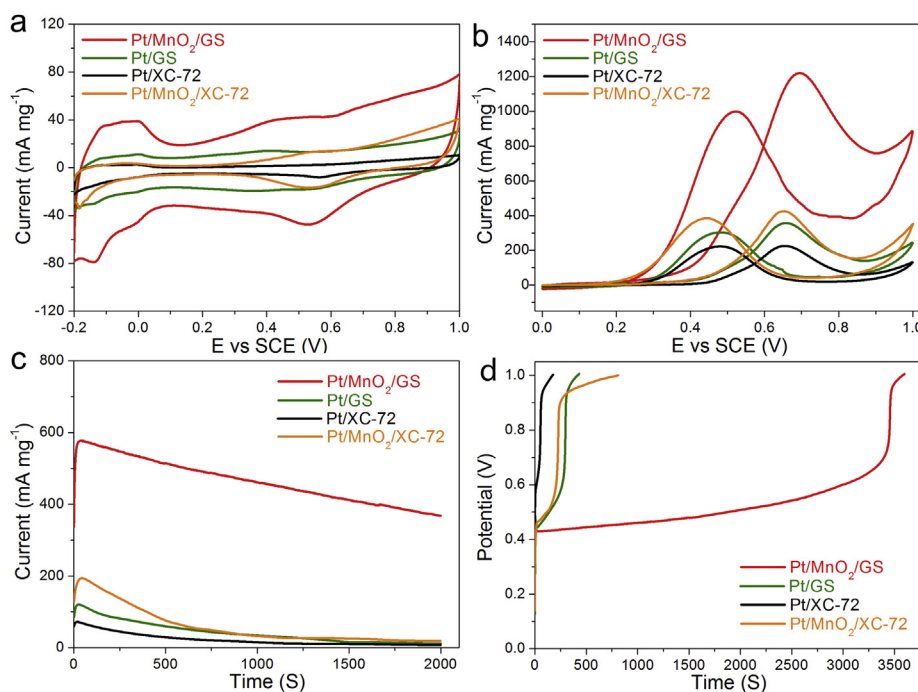
Fig. 3. (a) CVs of Pt/MnO$_2$/GS, Pt/GS, Pt/XC-72 and Pt/MnO$_2$/XC-72 in 1 M H$_2$SO$_4$ at 20 mV s^{-1}. (b) CVs of Pt/MnO$_2$/GS, Pt/GS, Pt/XC-72 and Pt/MnO$_2$/XC-72 in 1 M H$_2$SO$_4$ and 2 M methanol at 20 mV s^{-1}. (c) Chronoamperometric response recorded at 0.5 V (vs SCE) in 1 M H$_2$SO$_4$ and 2 M methanol for Pt/MnO$_2$/GS, Pt/GS, Pt/XC-72 and Pt/MnO$_2$/XC-72. (d) Chronopotentiometric curves of Pt/MnO$_2$/GS, Pt/GS, Pt/XC-72 and Pt/MnO$_2$/XC-72 in 1 M H$_2$SO$_4$ and 2 M methanol.

sheets are a promising support to improve the stability of Pt NPs and restrain the particle sizes through the strong interaction between MnO_2/GS support and Pt NPs. On the other hand, the chronopotentiometric technique, a useful approach for the evaluation of the catalysts toward methanol oxidation, was employed to further investigate the antipoisoning abilities of different catalysts. As seen in Fig. 3d, the electrode potential increases gradually for a certain time and then instantaneously reaches to a much higher potential for all catalysts. The sustained time for these catalysts decreases in the order Pt/MnO_2/GS ($\sim$3400 s) > Pt/GS ($\sim$300 s) > Pt/MnO_2/XC-72 ($\sim$220 s) > Pt/XC-72 ($\sim$50 s), consistent with the I_f/I_b values based on CV tests. The results further demonstrate the excellent electrochemical properties of Pt/MnO_2/GS, which meets the requirements of both high electrocatalytic activity and long cycling life for high-performance energy conversion devices.

Based on the results above, it can be deduced that the rational combination of Pt NPs, MnO_2 and graphene into a sophisticated 2D architecture is conducive to the development of high Pt utilization catalysts. A possible mechanism for the enhancement of electrochemical performance is proposed as follows [56–58]:

$$CH_3OH + Pt \rightarrow Pt - CO_{ads} + 4H^+ + 4e^- \qquad (1)$$

$$H_2O + MnO_2 \rightarrow MnO_2 - OH_{ads} + H^+ + e^- \qquad (2)$$

$$Pt - CO_{ads} + MnO_2 - OH_{ads} \rightarrow Pt + MnO_2 + CO_2 + H^+ + e^- \qquad (3)$$

First, the small-sized and well-dispersed Pt NPs on the modified carbon sheets can offer higher surface-areas that host more accessible active sites, thus achieving an extremely high electrocatalytic activity; Second, hydrous MnO_2 coating on graphene surface can facilitate the diffusion of electrolyte and also allow the transportation of the poisoning species and protons (H^+) from the Pt sites during the reaction [19,58]; Third, graphene sheets in the ternary composite act as not only the support for the deposition of Pt NPs but also the electronic conductive channels, leading to a significant decrease in charge-transfer resistance compared with XC-72-based catalysts (Fig. S8 and Table S3) and effectively improving the electrochemical kinetics.

4. Conclusions

In summary, a facile and cost-effective approach has been developed to disperse Pt NPs on MnO_2-functionalized graphene sheets. Graphene could be amazingly used as both a green reductant in synthesis of MnO_2 and an ideal substrate for growing and anchoring Pt NPs with a very narrow size distribution. Most importantly, the rationally designed Pt/MnO_2/GS ternary electrocatalyst exhibits ultrahigh electrocatalytic activity, good antipoisoning ability and exceptional long-term stability, significantly outperforming the Pt/GS, Pt/XC-72 and Pt/MnO_2/XC-72 catalysts. We believe this design concept can be extended to the fabrication of other novel nanocomposites containing noble metals, such as Pd, Au and Ag, opening up a brand new avenue for a large spectrum of device applications.

Acknowledgments

Appendix A. Supplementary data

Supplementary data related to this article can be found at http://dx.doi.org/10.1016/j.jpowsour.2013.03.133.

References

[1] A.S. Aricò, S. Srinivasan, V. Antonucci, Fuel Cells 1 (2001) 133–161.
[2] H.A. Gasteiger, N. Markovic, P.N. Ross, E.J. Cairns, J. Phys. Chem. 97 (1993) 12020–12029.
[3] H.S. Liu, C.J. Song, L. Zhang, J.J. Zhang, H.J. Wang, D.P. Wilkinson, J. Power Sources 155 (2006) 95–110.
[4] C. Huang, C. Li, G. Shi, Energy Environ. Sci. 5 (2012) 8848–8868.
[5] Y.H. Lin, X.L. Cui, C.H. Yen, C.M. Wai, Langmuir 21 (2005) 11474–11479.
[6] S.J. Liao, K.A. Holmes, H. Tsaprailis, V.I. Birss, J. Am. Chem. Soc. 128 (2006) 3504–3505.
[7] E. Antolini, J.R.C. Salgado, E.R. Gonzalez, J. Electroanal. Chem. 580 (2005) 145–154.
[8] H. Huang, Y. Fan, X. Wang, Electrochim. Acta 80 (2012) 118–125.
[9] Y. Kang, C.B. Murray, J. Am. Chem. Soc. 132 (2010) 7568–7569.
[10] Y. Kang, J.B. Pyo, X. Ye, T.R. Gordon, C.B. Murray, ACS Nano 6 (2012) 5642–5647.
[11] E. Casado-Rivera, D.J. Volpe, L. Alden, C. Lind, C. Downie, T. Vázquez-Alvarez, A.C.D. Angelo, F.J. DiSalvo, H.D. Abruña, J. Am. Chem. Soc. 126 (2004) 4043–4049.
[12] Y. Liu, D. Li, V.R. Stamenkovic, S. Soled, J.D. Henao, S. Sun, ACS Catal. 1 (2011) 1719–1723.
[13] S. Maksimuk, S. Yang, Z. Peng, H. Yang, J. Am. Chem. Soc. 129 (2007) 8684–8685.
[14] L. Cao, F. Scheiba, C. Roth, F. Schweiger, C. Cremers, U. Stimming, H. Fuess, L. Chen, W. Zhu, X. Qiu, Angew. Chem. Int. Ed. 45 (2006) 5315–5319.
[15] Y.-Y. Chu, Z.-B. Wang, Z.-Z. Jiang, D.-M. Gu, G.-P. Yin, Adv. Mater. 23 (2011) 3100–3104.
[16] H. Song, X. Qiu, D. Guo, F. Li, J. Power Sources 178 (2008) 97–102.
[17] J.S. Rebello, P.V. Samant, J.L. Figueiredo, J.B. Fernandes, J. Power Sources 153 (2006) 36–40.
[18] M.-W. Xu, G.-Y. Gao, W.-J. Zhou, K.-F. Zhang, H.-L. Li, J. Power Sources 175 (2008) 217–225.
[19] C. Zhou, H. Wang, F. Peng, J. Liang, H. Yu, J. Yang, Langmuir 25 (2009) 7711–7717.
[20] G.-Y. Zhao, H.-L. Li, Appl. Surf. Sci. 254 (2008) 3232–3235.
[21] J.J. Wang, G.P. Yin, J. Zhang, Z.B. Wang, Y.Z. Gao, Electrochim. Acta 52 (2007) 7042–7050.
[22] B. Wu, Y. Kuang, X. Zhang, J. Chen, Nano Today 6 (2011) 75–90.
[23] H. Huang, D. Sun, X. Wang, J. Phys. Chem. C 115 (2011) 19405–19412.
[24] K.S. Novoselov, A.K. Geim, S.V. Morozov, D. Jiang, Y. Zhang, S.V. Dubonos, I.V. Grigorieva, A.A. Firsov, Science 306 (2004) 666–669.
[25] Y.M. Li, L.H. Tang, J.H. Li, Electrochem. Commun. 11 (2009) 846–849.
[26] Y.J. Li, W. Gao, L.J. Ci, C.M. Wang, P.M. Ajayan, Carbon 48 (2010) 1124–1130.
[27] S. Sharma, A. Ganguly, P. Papakonstantinou, X.P. Miao, M.X. Li, J.L. Hutchison, M. Delichatsios, S. Ukleja, J. Phys. Chem. C 114 (2010) 19459–19466.
[28] A.K. Geim, K.S. Novoselov, Nat. Mater. 6 (2007) 183–191.
[29] S. Chen, J. Zhu, X. Wu, Q. Han, X. Wang, ACS Nano 4 (2010) 2822–2830.
[30] S. Chen, J. Zhu, X. Wang, ACS Nano 4 (2010) 6212–6218.
[31] H. Huang, X. Wang, Nanoscale 3 (2011) 3185–3191.
[32] C. Xu, X. Wang, J.W. Zhu, J. Phys. Chem. C 112 (2008) 19841–19845.
[33] H. Huang, H. Chen, D. Sun, X. Wang, J. Power Sources 204 (2012) 46–52.
[34] R. Liu, H. Zhou, J. Liu, Y. Yao, Z. Huang, C. Fu, Y. Kuang, Electrochem. Commun. 26 (2013) 63–66.
[35] W.S. Hummers, R.E. Offeman, J. Am. Chem. Soc. 80 (1958), 1339–1339.
[36] N.I. Kovtyukhova, P.J. Ollivier, B.R. Martin, T.E. Mallouk, S.A. Chizhik, E.V. Buzaneva, A.D. Gorchinskiy, Chem. Mater. 11 (1999) 771–778.
[37] G. Zhao, J. Li, L. Jiang, H. Dong, X. Wang, W. Hu, Chem. Sci. 3 (2012) 433–437.
[38] X. Jin, W. Zhou, S. Zhang, G.Z. Chen, Small 3 (2007) 1513–1517.
[39] Y. Omomo, T. Sasaki, L.Z. Wang, M. Watanabe, J. Am. Chem. Soc. 125 (2003) 3568–3575.
[40] Z.-h. Liu, X. Yang, Y. Makita, K. Ooi, Chem. Mater. 14 (2002) 4800–4806.
[41] S. Devaraj, N. Munichandraiah, J. Phys. Chem. C 112 (2008) 4406–4417.
[42] S. Chen, J. Zhu, Q. Han, Z. Zheng, Y. Yang, X. Wang, Cryst. Growth Des. 9 (2009) 4356–4361.
[43] Y. Hou, Y. Cheng, T. Hobson, J. Liu, Nano Lett. 10 (2010) 2727–2733.
[44] A.C. Ferrari, J. Robertson, Phys. Rev. B 61 (2000) 14095–14107.
[45] S. Stankovich, D.A. Dikin, R.D. Piner, K.A. Kohlhaas, A. Kleinhammes, Y. Jia, Y. Wu, S.T. Nguyen, R.S. Ruoff, Carbon 45 (2007) 1558–1565.
[46] A.C. Ferrari, J.C. Meyer, V. Scardaci, C. Casiraghi, M. Lazzeri, F. Mauri, S. Piscanec, D. Jiang, K.S. Novoselov, S. Roth, A.K. Geim, Phys. Rev. Lett. 97 (2006) 187401.
[47] T. Gao, M. Glerup, F. Krumeich, R. Nesper, H. Fjellvåg, P. Norby, J. Phys. Chem. C 112 (2008) 13134–13140.
[48] B.J. Tan, K.J. Klabunde, P.M.A. Sherwood, J. Am. Chem. Soc. 113 (1991) 855–861.
[49] R. Chetty, W. Xia, S. Kundu, M. Bron, T. Reinecke, W. Schuhmann, M. Muhler, Langmuir 25 (2009) 3853–3860.
[50] X. Wang, X. Li, D. Liu, S. Song, H. Zhang, Chem. Commun. 48 (2012) 2885–2887.

[51] H. Jiang, T. Zhao, C. Li, J. Ma, Chem. Commun. 47 (2011) 8590—8592.
[52] S.J. Guo, S.J. Dong, E.K. Wang, Adv. Mater. 22 (2010) 1269—1272.
[53] L. Wang, Y. Nemoto, Y. Yamauchi, J. Am. Chem. Soc. 133 (2011) 9674—9677.
[54] R. Lv, T. Cui, M.-S. Jun, Q. Zhang, A. Cao, D.S. Su, Z. Zhang, S.-H. Yoon, J. Miyawaki, I. Mochida, F. Kang, Adv. Funct. Mater. 21 (2011) 999—1006.
[55] S. Guo, S. Dong, E. Wang, ACS Nano 4 (2010) 547—555.
[56] H.A. Gasteiger, N.M. Markovic, P.N. Ross, J. Phys. Chem. 99 (1995) 8290—8301.
[57] A.V. Tripković, K.D. Popović, B.N. Grgur, B. Blizanac, P.N. Ross, N.M. Markovi&cacute, Electrochim. Acta 47 (2002) 3707—3714.
[58] C. Zhou, F. Peng, H. Wang, H. Yu, J. Yang, X. Fu, Fuel Cells 11 (2011) 301—308.